

Gamma Spectroscopy Lab Report

Vladimir Sheydorov

November 2025

Abstract

Gamma spectroscopy was performed using a NaI(Tl) scintillation detector to analyse emissions from ^{22}Na , ^{60}Co and ^{137}Cs . An energy calibration was established by fitting Gaussian photopeaks using Maximum Likelihood Estimation and applying orthogonal distance regression to account for uncertainties in both energy and channel number. This calibration was used to determine the annihilation photon energy from ^{22}Na , yielding a value of $509.0 \pm 0.3\text{ keV}$, which is 7 standard deviations away from the literature 511 keV . The detector energy resolution was found to improve with increasing photon energy, from $(9.44 \pm 0.09)\%$ at 511 keV to $(6.31 \pm 0.10)\%$ at 1332 keV .

The inverse-square dependence of gamma-ray intensity with distance from a point source was verified for the 511 keV peak over the range $160\text{--}450\text{ mm}$. In addition, coincidence measurements of the back-to-back annihilation photons revealed a strong angular correlation consistent with two-photon emission at 180° .

1 Introduction

Gamma-ray spectroscopy provides a powerful method for identifying radioactive isotopes and studying their decay processes. In this experiment the spectra of three sources were investigated: ^{22}Na , ^{60}Co , and ^{137}Cs , with particular emphasis on the 511 keV annihilation photons produced in ^{22}Na decay.

Three main objectives were addressed. First, an energy calibration of the detection system was performed using the well-known photopeaks of ^{60}Co and ^{137}Cs . By determining the centroid positions of these peaks in channel space and comparing them with their literature energies, a linear calibration curve $E = a + bn$ was established. This calibration was later used to determine the energy of the ^{22}Na annihilation peak and to assess the accuracy of the detector system.

The second part of the experiment examined how the detected intensity of 511 keV photons varies with distance from the source. By measuring the total counts under the annihilation peak at several detector–source separations, the expected inverse-square dependence was tested and quantitatively fitted.

Finally, the angular correlation between the two back-to-back 511 keV photons from positron annihilation was investigated. The coincidence intensity was measured as a function of detector angle, allowing the characteristic angular distribution to be observed.

Together, these measurements provide a comprehensive investigation of the detection, energy calibration, and angular behaviour of annihilation radiation, and they illustrate several important statistical and physical principles relevant to gamma-ray spectroscopy.

2 Theory

2.1 Na-22 decay

The decay scheme for ^{22}Na is shown in Figure 1. It can be seen in the diagram that 90.05% of the time ^{22}Na decay involves emission of a positron. Both in the 90% and the 0.05% cases when the positron annihilates with an electron, a pair of 511 keV gamma ray photons is produced [1]. These 511 keV gamma rays are used in all parts of the experiment.

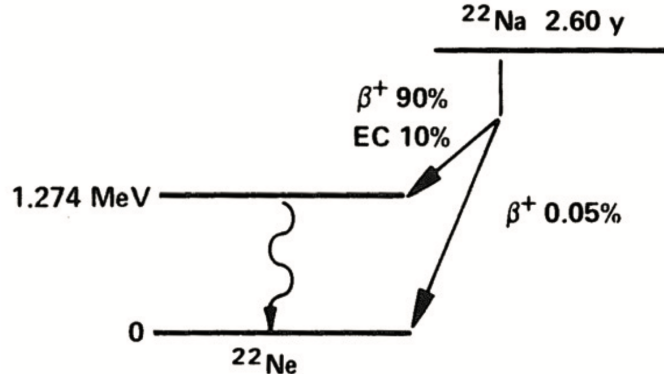


Figure 1: Decay scheme of ^{22}Na [1]

2.2 Scintillator, PMT, and MCA

Gamma rays are detected using a scintillation detector coupled to a photomultiplier tube (PMT). When a gamma photon deposits energy in the scintillator, it produces a burst of optical photons whose total light output is proportional to the deposited energy. This process is described in detail by Knoll [2]. The scintillation light is converted into photoelectrons at the photocathode of the PMT and subsequently multiplied through a dynode chain, producing an electrical pulse whose amplitude is proportional to the gamma-ray energy.

The pulse is analysed by a multichannel analyser (MCA), which digitises the pulse height and assigns it to one of many discrete channels. The MCA thus constructs a histogram of counts versus channel number, forming the gamma-ray energy spectrum. A detailed description of MCA operation and pulse processing can be found in Gilmore [3]. The finite energy resolution of the scintillator–PMT system leads to approximately Gaussian photopeaks, arising from statistical fluctuations in photon production and electron multiplication [2].

2.3 Poisson statistics in radiation detection

Radioactive decay is a fundamentally random process, and the detection of gamma rays therefore follows Poisson statistics. If the mean number of photons detected in a given channel during a fixed acquisition time is λ , the probability of observing N counts is

$$P(N | \lambda) = \frac{\lambda^N e^{-\lambda}}{N!}.$$

A characteristic feature of the Poisson distribution is that the variance is equal to the mean, $\sigma^2 = \lambda$. As a consequence, the statistical uncertainty on a measured count rate is well approximated by

$$\sigma_N \approx \sqrt{N}.$$

In gamma-ray spectroscopy this behaviour arises because each detected photon is an independent event, and the arrival of photons at the detector is a memoryless process [4]. At sufficiently high count rates, the Poisson distribution approaches a Gaussian with standard deviation $\sigma = \sqrt{N}$, which is often used as a practical approximation. The Poisson nature of the data underlies the choice of statistical models used in the analysis, including the use of likelihood methods for peak fitting.

2.4 Detector Resolution

In an ideal detector each monoenergetic gamma ray would produce a pulse of identical height, resulting in a delta-function photopeak. In practice, scintillation detectors exhibit a finite energy resolution, meaning that photopeaks acquire a characteristic width. The dominant contribution arises from statistical fluctuations in the number of scintillation photons produced and the number of photoelectrons generated at the PMT photocathode. Since these processes follow Poisson-like statistics, the relative fluctuation decreases only as $1/\sqrt{N}$, where N is the number of detected photons [2].

As a result, the distribution of pulse heights for monoenergetic gamma rays is well approximated by a Gaussian with standard deviation σ and centroid E_0 . The energy resolution is commonly expressed as

$$\frac{\Delta E}{E_0} = \frac{2.355 \sigma}{E_0},$$

where ΔE is the full width at half maximum (FWHM). This finite resolution explains the width of the peaks observed in this experiment, and provides theoretical justification for modelling the photopeaks using Gaussian functions with a linear background.

2.5 Inverse-square law

A radioactive point source emits gamma rays isotropically. As these photons spread out uniformly in three dimensions, the same number of particles is distributed over the surface of a sphere of radius r . The photon flux is therefore proportional to the surface area [2],

$$I(r) \propto \frac{1}{4\pi r^2},$$

giving the inverse-square dependence

$$I(r) \propto \frac{1}{r^2}.$$

This relationship holds when the detector is sufficiently far from the source such that both can be approximated as point-like (the far-field limit). At short distances, deviations may occur due to finite detector size, finite source size, and geometric alignment [5].

2.6 Positron-electron annihilation

When the ^{22}Na positrons are annihilated from colliding with an electron, two 0.511 MeV gamma-rays photons are emitted with an angular separation of $\sim 180^\circ$. The 0.511 MeV gamma ray energy being equal to the rest energy of an electron or positron [6].

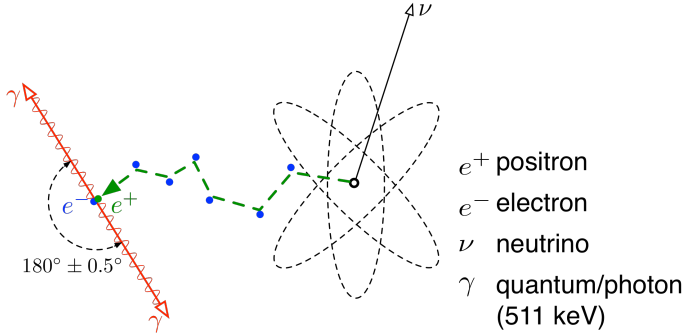


Figure 2: Naturally occurring electron-positron annihilation as a result of beta plus decay [7]

The ^{22}Na source was encapsulated in a plastic holder. Positrons emitted in the decay have a mean range of approximately 1.5 mm in Lucite (acrylic) [8]. Therefore, virtually all positrons annihilate within a few millimetres of their point of emission, and the resulting 511 keV photons can be treated as originating from a single, effectively point-like location within the source.

3 Experimental Method

Gamma-ray spectra were recorded using sealed ^{60}Co , ^{137}Cs and ^{22}Na sources. Detection was performed with a 1-inch NaI(Tl) scintillation detector coupled to a photomultiplier tube (PMT) [9]. The PMT output was fed into an ORTEC 4890 preamplifier–amplifier–SCA unit, and the resulting analogue pulses were sent to a multichannel analyser (MCA), which sorted events into channels according to pulse height. For all experiments two blocks of lead (wrapped in aluminium foil) were used to help minimize the amount of background radiation.

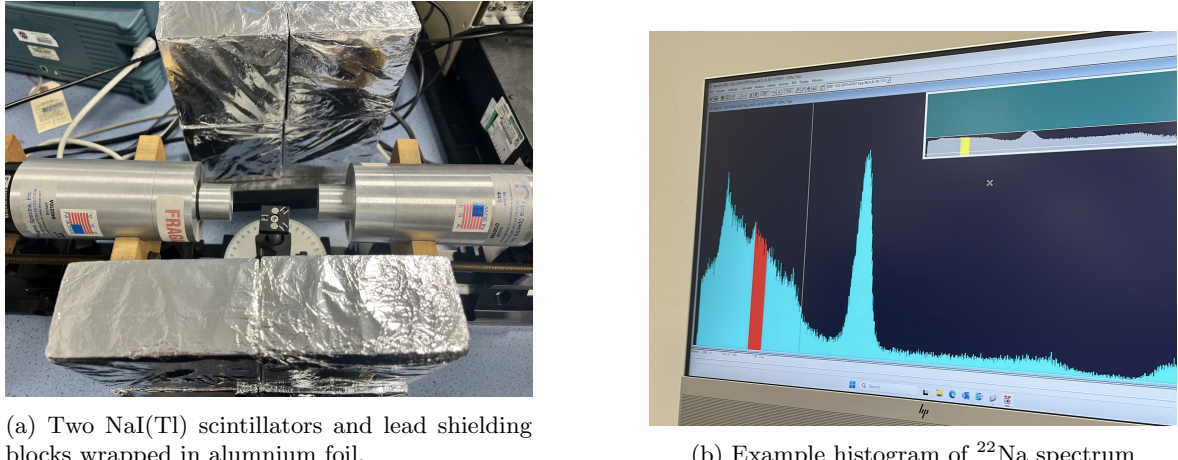


Figure 3: Experimental Setup

Energy calibration

For the calibration measurements the amplifier coarse gain was set to 8, with the fine gain at its minimum value. This ensured best capture of peaks for the calibration part of the experiment.

The MCA lower and upper discriminators were adjusted to include each photopeak of interest while excluding the majority of the surrounding spectrum. This ensured dead-time remained below 1%, making dead-time losses negligible. A real-time acquisition of 1800 seconds was used for each source. The relevant peaks were the 662 keV of ^{137}Cs , the 1173 keV and 1332 keV of ^{60}Co , and the 511 keV annihilation peak of ^{22}Na .

Inverse-square law measurements

To investigate the distance dependence of gamma-ray intensity, the amplifier settings were kept fixed throughout. Spectra of the 511 keV peak from ^{22}Na were recorded at relative detector–source separations of 160, 200, 250, 300, 350, 400 and 450 mm, as indicated by the scale on the detector stand. These values represent consistent relative distances rather than absolute centre-to-centre separations. The closest position (160 mm) was chosen such that the true detector–source distance exceeded approximately three times the scintillator diameter, minimising near-field effects and ensuring the validity of the far-field inverse-square approximation. Each spectrum was measured for real time of 300 seconds.

Angular dependence of coincidence detection

In the final part of the experiment, the angular correlation of the back-to-back annihilation photons from ^{22}Na was measured. When a positron annihilates at rest, two 511 keV gamma rays are emitted approximately 180° apart. This was investigated using a fixed detector and a second detector mounted on a rotating arm centred on the source. Figure 4 illustrates the geometry of the rotating assembly.

Coincidence spectra were recorded at detector angles of -20° , -15° , -10° , -7° , -5° , 0° , 5° , 7° , 10° , 15° and 20° . At each angle, the number of coincident 511 keV events was measured.

The coincidence electronics consisted of an ORTEC 416A gate generator, an ORTEC 427A delay amplifier, and the gate input of the MCA, which ensured that only temporally correlated pulses from the two detectors were recorded as coincidences. A real-time acquisition of 300 seconds was used. The absolute distance of detector–source was kept at ~ 65 mm.

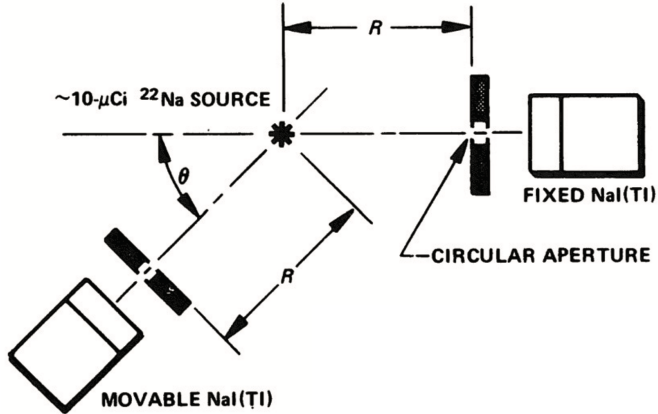


Figure 4: The Mechanical Arrangement of the Source, Apertures and Detectors on the Angular Correlation Table [1].

4 Results

4.1 General

The data collected was stored in .Spe ASCII files and can be accessed through the provided supplementary material. The python code used to perform the data analysis can also be accessed in the supplementary materials. It is written so that it can be run on any machine. Refer to Appendix B for more information.

Data points for first and last non zero counts were removed from the spectrum and data analysis for all collected data, as they were often anomalous. For some data additional truncating may have been done to further isolate the peak and remove the surroundings. For instance, further truncation was done in code to remove any potential Compton surrounding spectrum when doing calibration fitting on Sodium, Caesium and Cobalt.

Several sources of uncertainty affect the collected data. The primary source of statistical uncertainty arises from the inherent counting nature of the detector. Since photon detection follows Poisson statistics, the uncertainty on each measured count N is taken to be \sqrt{N} . These Poisson error bars are applied consistently throughout all analyses, including peak fitting, calibration, and activity estimation. Instrumental sources of error include electronic noise, finite energy resolution of the detector, and potential gain drift over time.

Overall, the combination of careful data cleaning, truncation where appropriate, and consistent application of Poisson statistics ensures that the reported results are as accurate and reliable as possible within the limitations of the experimental setup.

4.2 Calibration

Peak centroids were obtained by fitting Gaussians with linear background using Maximum Likelihood Estimation (MLE), where for each bin $P(N | \lambda)$ is assumed to follow a Poisson probability distribution (Fig. 5, 7, 8). A detailed discussion of likelihood methods and uncertainty determination can be found in Cowan [10]. Centroid errors were estimated from the covariance matrix obtained by inverting the Hessian of the log-likelihood at the MLE solution. See gamma_calibration.py for this part.

After determining peak centroids, orthogonal distance regression (ODR) [11] was used to do the calibration linear plot of $E = a + bn$, since least squares can't take into account the non-negligible error of independent variable n . This way an error on a and b (and their covariance matrix) can be obtained. The linear plot is shown in Fig. 9.

The final energy of the ^{22}Na 511 keV annihilation photon was obtained by propagating uncertainties from both the calibration parameters and the measured ^{22}Na centroid. Monte Carlo sampling was used for this propagation, following the general methodology described by Cowan [12].

The MLE fits to the three calibration spectra produced reduced χ^2 values in the range 1.06–1.24.

4.2.1 ^{137}Cs centroid

For ^{137}Cs , the 0.662 MeV photopeak was measured. A Gaussian with a linear background was fitted using MLE. The fitted rate equation is of the form: $R(n) = |A_1 + A_2(n - A_4)| + |A_3| \exp(-0.5 \frac{(n - A_4)^2}{A_5^2})$. The parameters A_4 , A_5 (0.662 MeV peak centroid and standard deviation) were found to be:

$$A_4 = 252.99 \pm 0.03,$$
$$A_5 = 9.11 \pm 0.03.$$

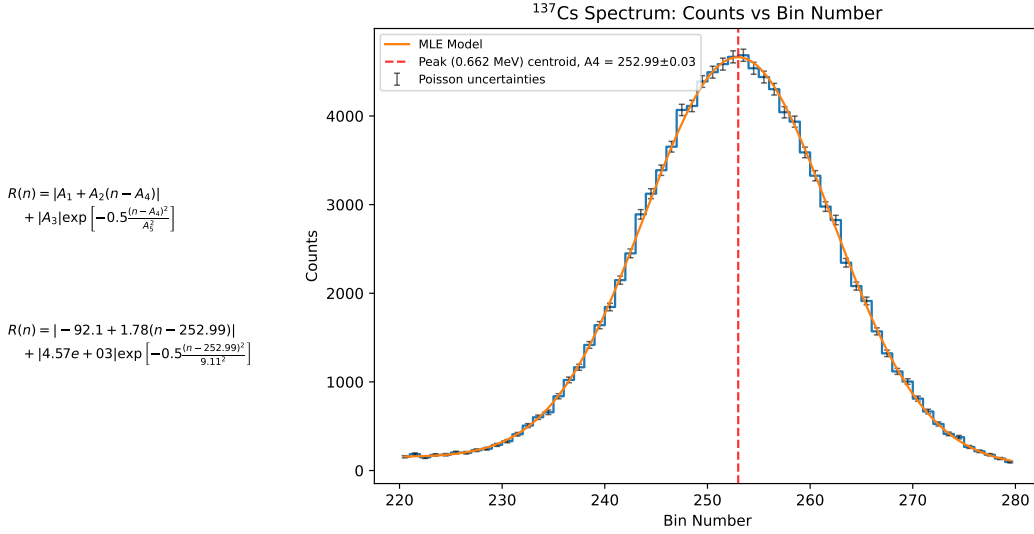


Figure 5: MLE fit of a Gaussian with linear background for ^{137}Cs spectrum. $\chi^2 = 58.1$, reduced $\chi^2 = 1.057$ (dof = 55)

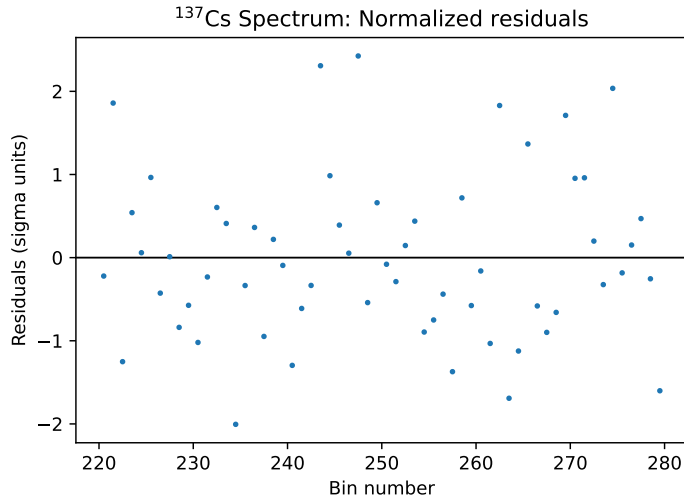


Figure 6: Normalized residuals of MLE fit for ^{137}Cs spectrum. The residuals show no systematic trends and scatter randomly around zero, indicating the model provides a good fit to the observed data. This is also true for ^{60}Co and ^{22}Na fit residuals, and can be confirmed by the reader in Appendix A, Fig.17 and 18.

4.2.2 ^{60}Co centroid

For ^{60}Co , the 1.17 MeV and 1.33 MeV photopeaks were measured. The following rate equation was fitted using MLE: $R(n) = |A_1 + A_2(n - A_4)| + |A_3| \exp(-0.5 \frac{(n - A_4)^2}{A_5^2}) + |A_6| \exp(-0.5 \frac{(n - A_7)^2}{A_8^2})$. The parameters A_4, A_5 (1.17MeV peak centroid and standard deviation) and A_7, A_8 (1.33MeV centroid

and standard deviation) were found to be:

$$A_4 = 441.6 \pm 0.4,$$

$$A_5 = 12.0 \pm 0.7,$$

$$A_7 = 500.9 \pm 0.5,$$

$$A_8 = 13.2 \pm 0.3.$$

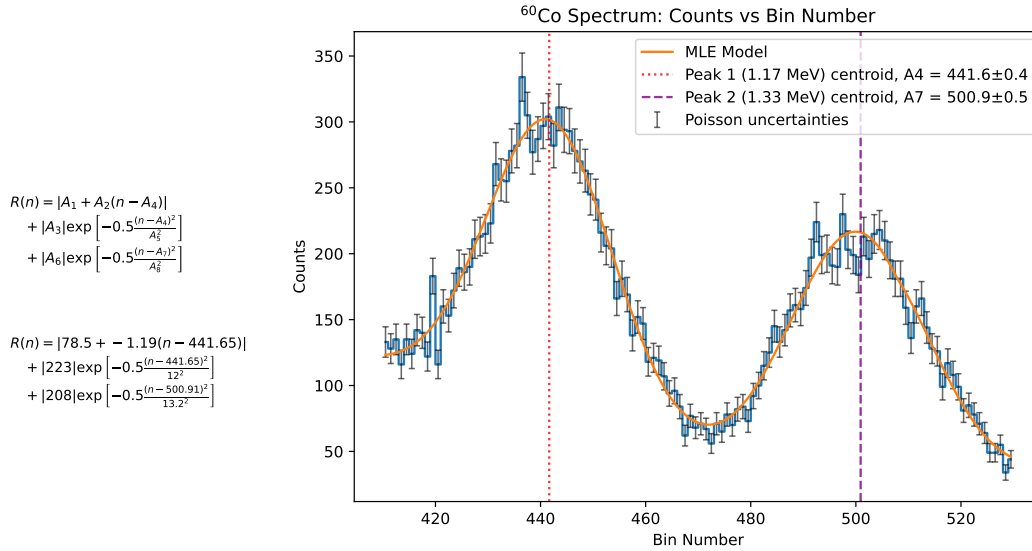


Figure 7: MLE fit of a Gaussian with linear background for ^{60}Co spectrum. $\chi^2 = 119.5$, reduced $\chi^2 = 1.067$ (dof = 112). To see the residuals refer to Appendix A, Fig 17

4.2.3 ^{22}Na centroid

For ^{22}Na , the 0.551 MeV photopeak was measured. A Gaussian with a linear background was fitted using MLE. The fitted rate equation is of the form: $R(n) = |A_1 + A_2(n - A_4)| + |A_3| \exp(-0.5 \frac{(n - A_4)^2}{A_5^2})$. The parameters A_4 and A_5 (511 keV centroid and standard deviation) were found to be:

$$A_4 = 196.62 \pm 0.07,$$

$$A_5 = 7.56 \pm 0.07.$$

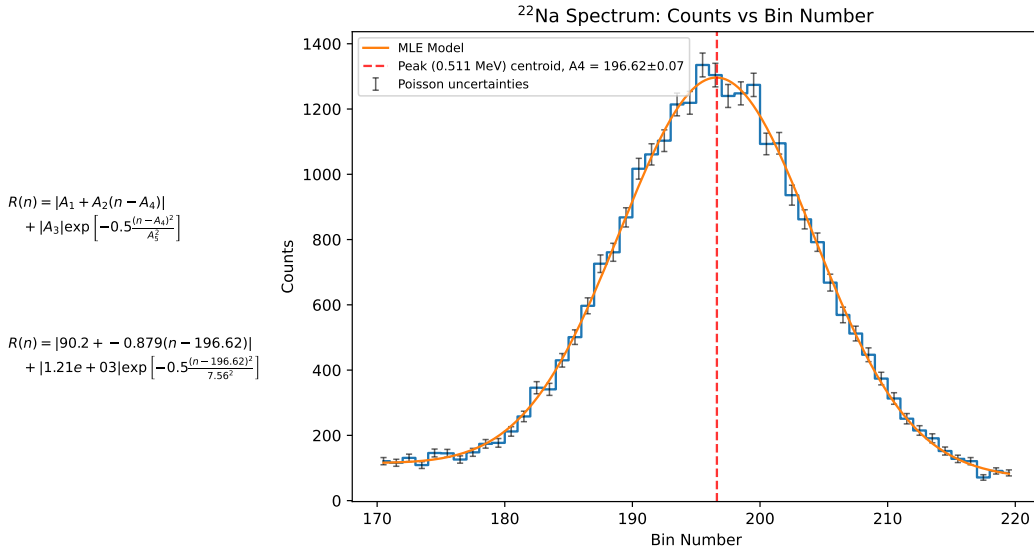


Figure 8: MLE fit of a Gaussian with linear background for ^{22}Na spectrum. $\chi^2 = 55.6$, reduced $\chi^2 = 1.236$ (dof = 45). To see the residuals refer to Appendix A, Fig 18.

4.2.4 Inferring ^{22}Na energy

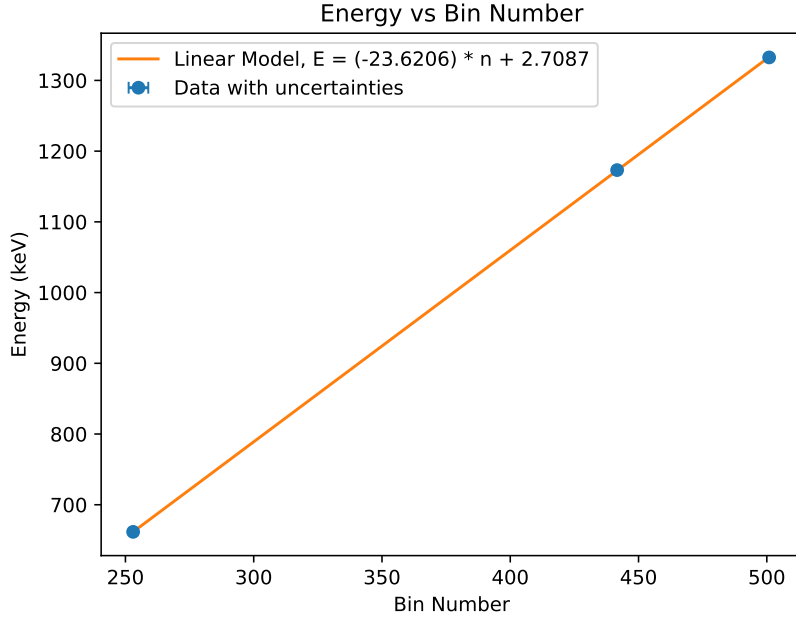


Figure 9: Linear plot of energy vs bin number. The model equation being $E = a + bn$. Vertical (energy) uncertainties were assumed to be negligible. Horizontal uncertainties are the found uncertainties on centroid positions. The constants a and b , and their uncertainties were found using Orthogonal Distance Regression (ODR). $a = -23.6 \pm 1.0$ keV, $b = 2.708 \pm 0.004$ keV/bin.

Using the ODR fitted energy calibration model, and also using Monte Carlo error propagation the final energy of the ^{22}Na 511keV photo-peak was found to be 509.0 ± 0.3 keV.

4.2.5 Detector energy resolution

Detector resolution for different energies was calculated using the standard deviation of the fitted peaks.

Expressed as percentages, the detector energy resolutions are:

$$\text{Resolution at } 511.0 \text{ keV: } R = (9.44 \pm 0.09)\%,$$

$$\text{Resolution at } 661.657 \text{ keV: } R = (8.79 \pm 0.03)\%,$$

$$\text{Resolution at } 1173.2 \text{ keV: } R = (6.5 \pm 0.4)\%,$$

$$\text{Resolution at } 1332.5 \text{ keV: } R = (6.3 \pm 0.1)\%.$$

4.3 Compton Edge Identification

Although the theoretical Compton edge for the 511 keV photon from ^{22}Na is well defined ($E_{\text{CE}} \approx 0.34$, MeV), it could not be confirmed experimentally under the calibrated conditions used in this study. The gain settings for the ^{22}Na calibration spectrum were optimized for the 511 keV photopeak, meaning that the lower-energy region containing the Compton continuum and edge (approximately 150–350 keV) fell outside the acquisition window. A separate ^{22}Na spectrum recorded with a lower gain clearly showed the Compton edge, but it could not be used quantitatively because calibration requires a single fixed gain for all spectra; applying the calibration derived from the ^{60}Co and ^{137}Cs spectra to a differently scaled dataset would introduce systematic error. Therefore, although Compton scattering was qualitatively visible in the high-gain measurement, the Compton edge could not be validated quantitatively under calibrated conditions; this does not affect the accurate identification of the 511 keV annihilation peak.

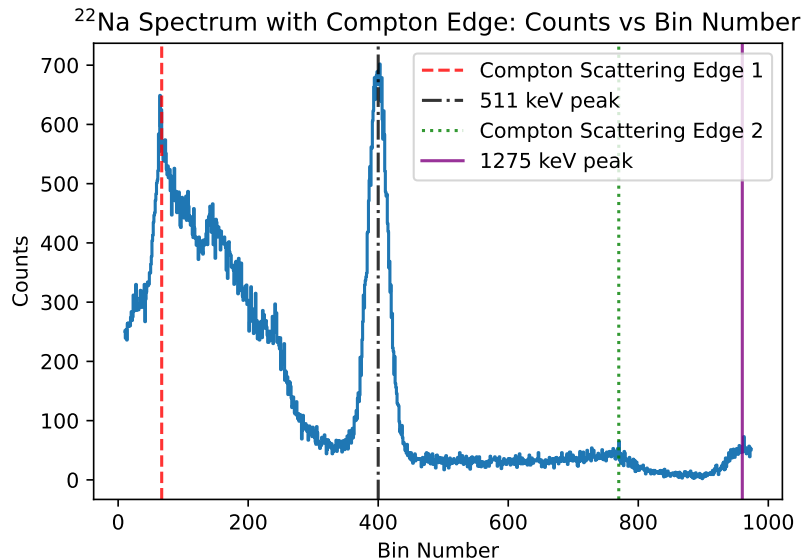


Figure 10: ^{22}Na spectrum with 511 keV, 1275 keV peaks and their respective Compton edges visible

4.4 Inverse square behavior of intensity

The data collected was modeled by $I(r) = \frac{k}{(r+r_0)^2} + b$, where r is relative detector-source distance, b is background radiation, k is proportionality constant. For this model MLE was not used, as k would tend to stay the same as the initial guessing parameter. Least squares fitting was used here instead. See Appendix B, Fig. (21-27) to see how the Intensity was calculated. See `inverse_square.py`.

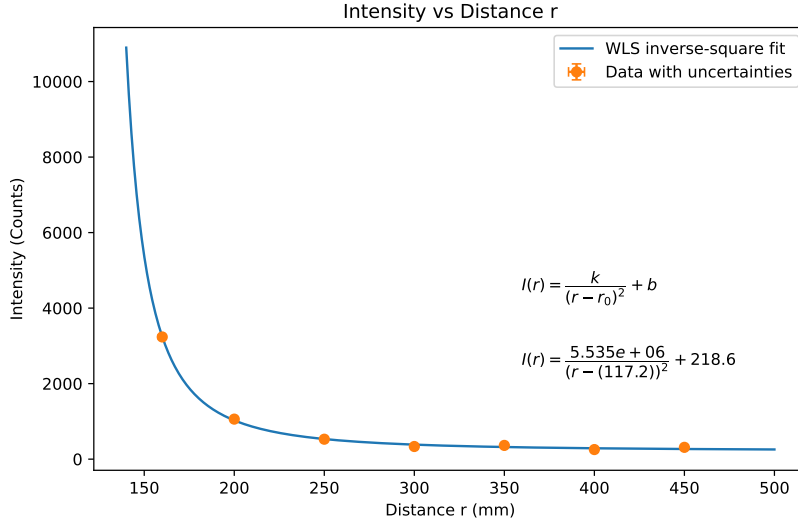


Figure 11: Least squares fit for Intensity vs Distance. $\chi^2 = 24.317$, reduced $\chi^2 = 6.079$ (dof = 4)

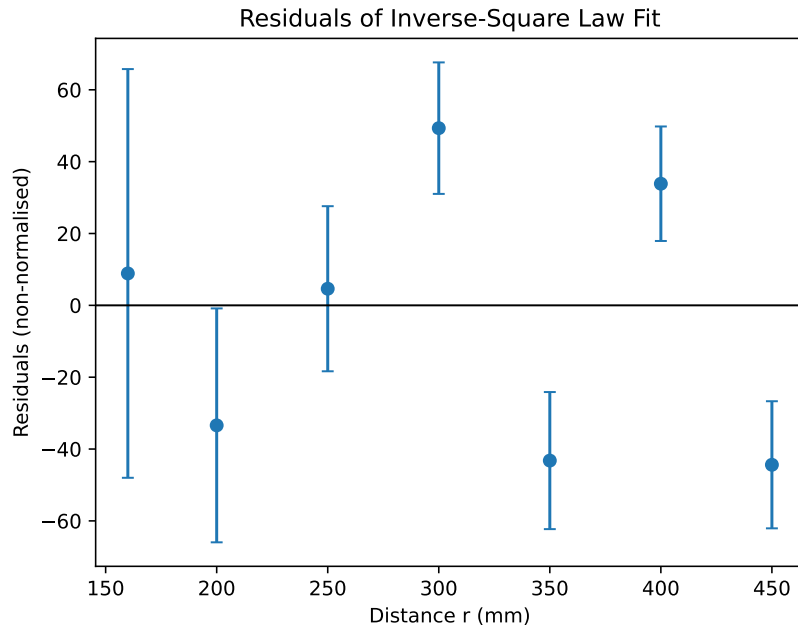


Figure 12: Residuals for Inverse square fit. Residuals show no systematic structure and are randomly scattered about zero, indicating that the fit adequately describes the data. The normalized residuals plot can be found in Appendix A, Figure 19.

4.5 Angular dependence of the coincident intensity.

The data collected was found to be best described by a Gaussian with no background: $R(\theta) = |A| \exp[-0.5 \frac{(n-x_0)^2}{s^2}]$. MLE was used to perform the model fit. See coincidence_angles.py for this part.

To calculate the coincidence intensity the bin window was set to [175, 230] as seen in Figure 13, and the total number of counts in that range was found.

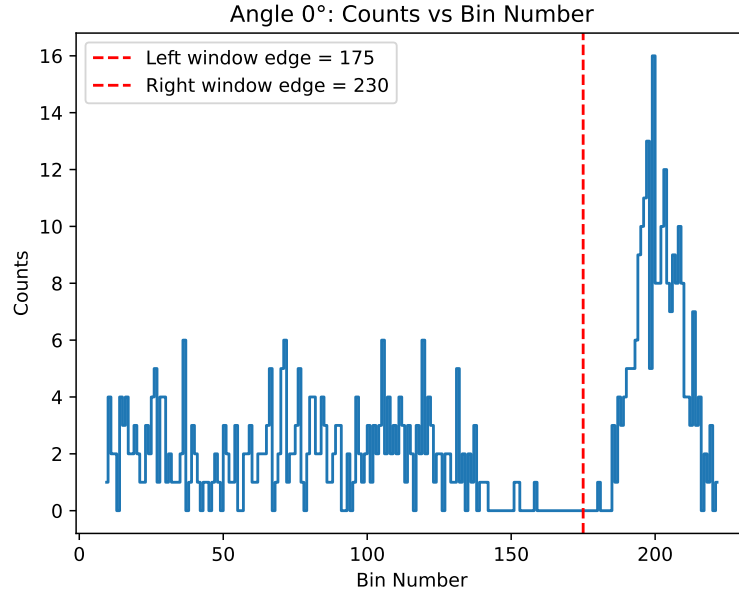


Figure 13: Example of how the counts were calculated for angle of 0 degrees. The red lines enclose the 511keV coincidence peak. The total count of 221(15) is found by adding all the recorded counts between the red lines. Integration window is kept constant between 175 and 230 for every angle. It can be seen in Appendix A (Fig 28 - 38) that the selected boundary successfully encloses the peaks for different angles.

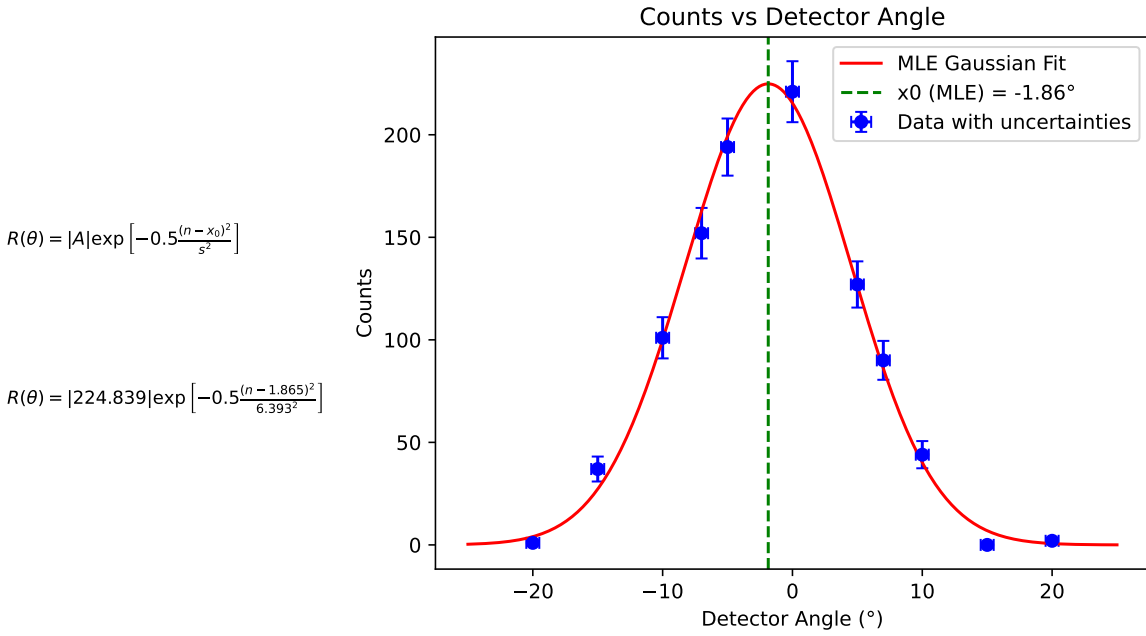


Figure 14: Counts vs detector angle. The model equation $R(\theta)$ is a gaussian with no background. $\chi^2 = 17.095$, reduced $\chi^2 = 2.137$ (dof = 8). The peak offset is given by $x_0 = 1.9 \pm 0.2$ degrees. Vertical uncertainty of data is Poisson. Horizontal is $\pm 0.5^\circ$ which is half the used scaling.

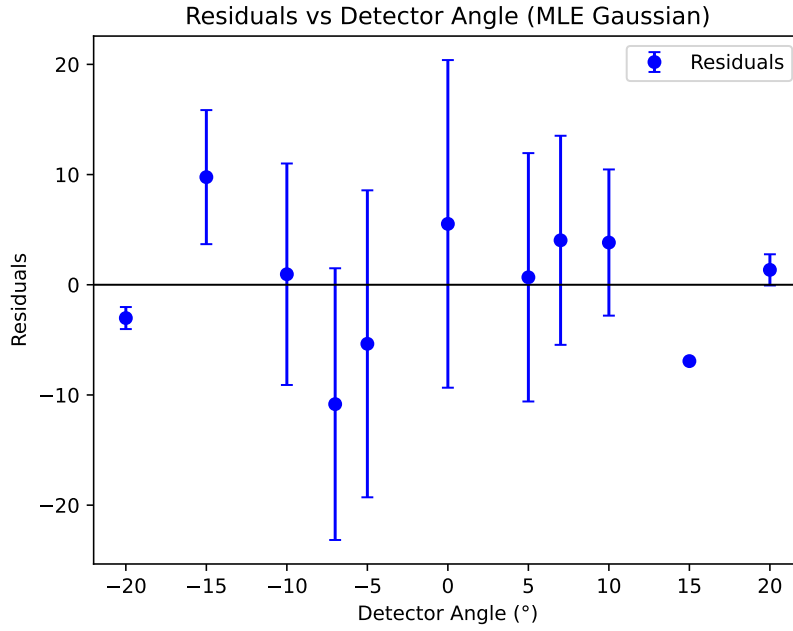


Figure 15: Residuals for counts vs angle. Residuals show no systematic structure and are randomly scattered about zero, indicating that the fit adequately describes the data.

5 Discussion

The calibration fits using Maximum Likelihood Estimation produced reduced χ^2 values in the range 1.06–1.24, indicating statistically acceptable, well-behaved models. The normalized residuals show no systematic trend and are randomly distributed around zero, consistent with correctly estimated Poisson uncertainties. Although least-squares regression typically yields lower χ^2 values when Gaussian errors are assumed, MLE is statistically more appropriate for spectral data because each channel count follows a Poisson distribution, particularly in low-count regions where Gaussian approximations fail.

In the ^{60}Co calibration spectrum, the 1.17 MeV and 1.33 MeV photopeaks overlap due to the finite resolution of the NaI(Tl) detector. A simultaneous two-Gaussian fit with a shared linear background was therefore used rather than attempting to isolate the peaks manually. This method avoids bias from arbitrary truncation and yields physically meaningful centroid estimates; the resulting reduced $\chi^2 = 1.057$ confirms the adequacy of the model.

The extracted ^{22}Na annihilation photon energy was found to be 508.96 ± 0.28 keV, which differs from the literature value of 511 keV by approximately 7 standard deviations. This strongly suggests a systematic shift in the calibration parameters. A likely contribution is unmonitored PMT and amplifier gain drift over the course of the experiment, since all spectra were acquired at different times and the gain stability was not checked with a reference source. Differential non-linearity and bin-width uncertainties are expected to be negligible in comparison [13].

The detector energy resolution improves with increasing γ -energy, from $(9.44 \pm 0.09)\%$ at 511 keV to $(6.31 \pm 0.10)\%$ at 1332 keV. This behaviour is consistent with Poisson statistics: higher-energy photons generate a greater number of scintillation photons and photoelectrons, reducing fractional statistical fluctuations and therefore narrowing the peaks.

In the inverse-square experiment, the general decrease in counts with distance follows the expected $1/r^2$ behaviour. The model fit gives reduces χ^2 of 6.079 indicating a potentially inaccurate fit. The counting method most likely introduces increasing statistical uncertainty at large distances, reducing peak extraction accuracy.

The coincidence angular distribution exhibits a clear maximum near 180° , confirming back-to-back photon emission from positron-electron annihilation. The fitted Gaussian width reflects the finite detector size and alignment tolerances rather than any intrinsic spread in emission angle. A small offset of the fitted centre ($x_0 \approx 1.8^\circ$) is attributed to imperfect detector positioning and non-parallel orientation of the scintillator faces. The χ^2 of 2.137 suggests the Gaussian is a reasonable model to describe the phenomena.

Uncertainties, limitations, and potential improvements

- The Compton edge could not be quantitatively analysed under calibrated conditions due to the restricted energy window used during acquisition.
- MCA energy windowing may remove useful background information that would improve fitting stability.
- Gain stability was not monitored over time, contributing to the calibrated energy shift.
- Detector positioning in the coincidence setup lacked mechanical precision, affecting the fitted

angular offset.

Future improvements include: securing detector alignment and distance more reliably; measuring calibration spectra both before and after data collection to monitor gain drift; acquiring spectra over wider energy ranges to retain the Compton continuum; increasing measurement times for improved statistics; and, where available, repeating key measurements with a high-resolution HPGe detector to reduce peak overlap effects.

6 Conclusion

The experiment successfully demonstrated several key properties of gamma radiation and the behaviour of a NaI(Tl) scintillation detection system. Energy calibration was achieved using well-known photopeaks from ^{137}Cs and ^{60}Co , and the calibration was applied to the ^{22}Na annihilation peak, yielding a measured photon energy of $508.96 \pm 0.28\text{ keV}$. Although slightly lower than the literature value of 511 keV , this difference is attributed to systematic effects such as amplifier gain drift. The measured detector energy resolution improved from $(9.44 \pm 0.09)\%$ at 511 keV to $(6.31 \pm 0.10)\%$ at 1332 keV , consistent with the expected increase in scintillation light yield for higher-energy photons.

The inverse-square experiment confirmed that photon intensity decreases approximately as $1/r^2$ with distance, validating the point-source approximation in the far field. The coincidence measurement demonstrated the expected angular correlation of positron–electron annihilation photons, with a clear maximum near 180° in the coincidence counting rate.

Overall, the experimental results are in good agreement with theoretical expectations within statistical and systematic uncertainties, and illustrate the capabilities and limitations of NaI(Tl)-based gamma spectroscopy in nuclear measurements.

References

- [1] ORTEC. Experiment 13: Gamma-gamma coincidence with angular correlation. <https://www.ortec-online.com/-/media/ametekortec/third-edition-experiments/13-gamma-gamma-coincidence-angular-correlation.pdf>.
- [2] Glenn F. Knoll. *Radiation Detection and Measurement*. Wiley, Hoboken, NJ, 4 edition, 2010. See Chapter 2, discussion of geometrical efficiency and inverse-square behaviour.
- [3] Gordon Gilmore. *Practical Gamma-Ray Spectrometry*. John Wiley & Sons, Chichester, 2 edition, 2008. Covers MCA systems, peak analysis, and detector operation.
- [4] Glenn F. Knoll. *Radiation Detection and Measurement*. Wiley, Hoboken, NJ, 4 edition, 2010. See Chapter 3: statistical fluctuations of radioactive counts follow a Poisson distribution.
- [5] Glenn F. Knoll. *Radiation Detection and Measurement*. Wiley, Hoboken, NJ, 4 edition, 2010. See Section 2.7: deviation from inverse-square law at short distances due to finite detector geometry.
- [6] M. Charlton and J. Humberston. *Positron Physics*. Cambridge University Press, 2009.
- [7] Wikipedia contributors. Electron–positron annihilation. https://en.wikipedia.org/wiki/Electron%20%93positron_annihilation. Accessed: 2025-02-12.
- [8] University of Wisconsin–Milwaukee. Radionuclide safety data sheet for na-22. <https://uwm.edu/safety-health/wp-content/uploads/sites/405/2016/11/Na-22.pdf>. Accessed: 2025-02-12.
- [9] Alpha Spectra, Inc. Integral type: Cylindrical and rectilinear. <https://alphaspectra.com/products/integral/>. Scintillator model 4I4/2, crystal diameter of 1 inch, Accessed: 2025-02-12.
- [10] Glen Cowan. *Statistical Data Analysis*. Oxford University Press, Oxford, 1998. Chapter 6 covers Maximum Likelihood Estimation and likelihood-based uncertainty determination.
- [11] SciPy Developers. scipy.odr — orthogonal distance regression (odrpack). <https://docs.scipy.org/doc/scipy/reference/odr.html>. Accessed 2025-12-02.
- [12] Glen Cowan. *Statistical Data Analysis*. Oxford University Press, Oxford, 1998. Chapter 3 — Monte Carlo techniques.
- [13] D. A. Gedcke. How histogramming and counting statistics affect peak position precision. <https://www.ortec-online.com/-/media/ametekortec/application-notes/an58.pdf?la=en&revision=4a94e5c4-a8c3-4955-8760-595610345e0b&hash=D57AE6A30882539409E0A40A456392F0>. Conclusions on page 9 states the conditions for different errors to be considered, Accessed 2025-12-02.

A Additional Plots

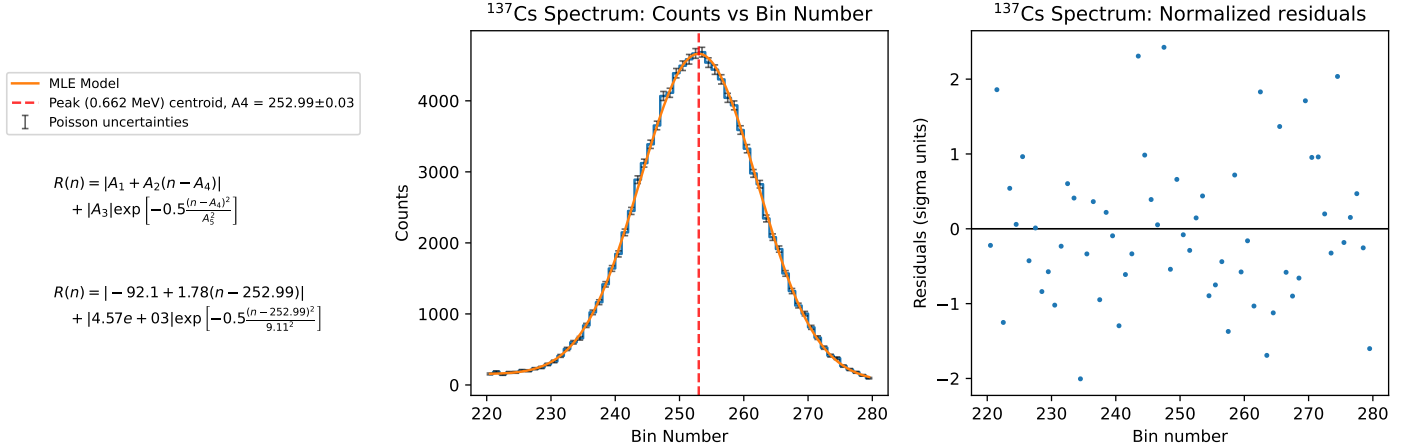


Figure 16: MLE fit for ^{137}Cs spectrum, and normalized residuals. $\chi^2 = 58.1$, reduced $\chi^2 = 1.057$ (dof = 55). Negative log-likelihood of MLE: 292.32. $A_1 = -92 \pm 5$, $A_2 = 1.78 \pm 0.15$, $A_3 = (4.57 \pm 0.02) \times 10^3$, $A_4 = 252.99 \pm 0.03$, $A_5 = 9.11 \pm 0.03$.

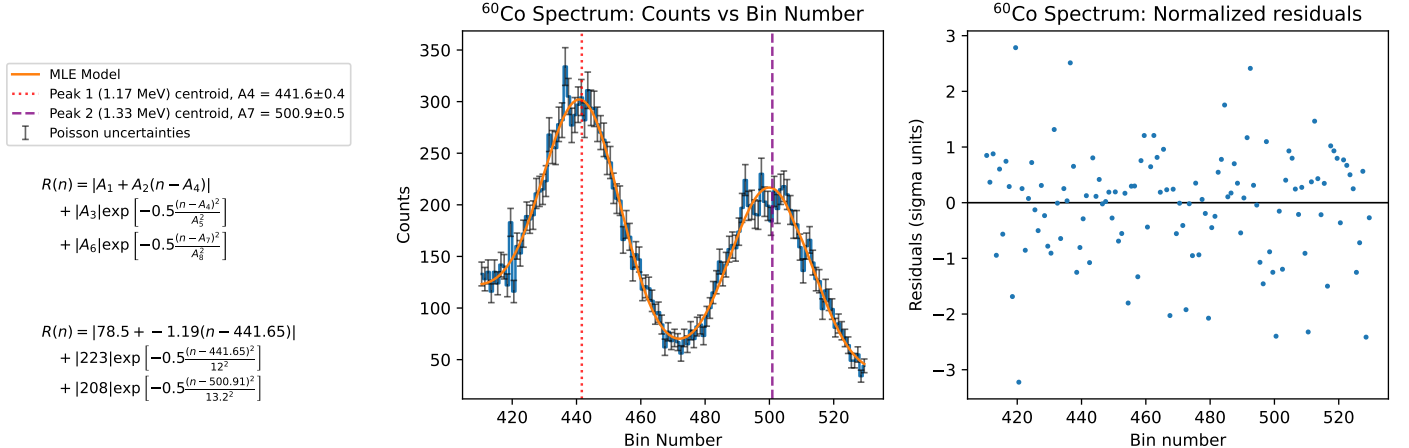


Figure 17: MLE fit for ^{60}Co spectrum, and normalized residuals. $\chi^2 = 119.5$, reduced $\chi^2 = 1.067$ (dof = 112). Negative log-likelihood of MLE: 466.7. $A_1 = 78.5 \pm 9.2$, $A_2 = -1.19 \pm 0.12$, $A_3 = 223 \pm 8$, $A_4 = 441.65 \pm 0.37$, $A_5 = 11.98 \pm 0.71$, $A_6 = 208 \pm 4$, $A_7 = 500.91 \pm 0.47$, $A_8 = 13.18 \pm 0.28$.

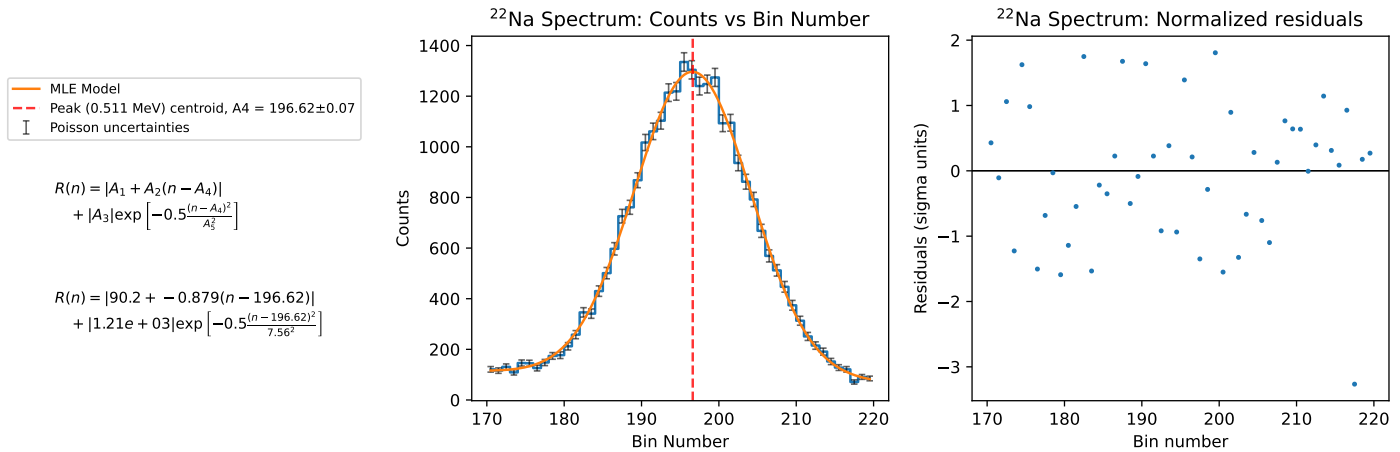


Figure 18: MLE fit for ^{22}Na spectrum, and normalized residuals. $\chi^2 = 55.6$, reduced $\chi^2 = 1.236$ (dof = 45). Negative log-likelihood of MLE: 221.08. One residual deviates 3σ , which is most likely consistent with expected statistical fluctuations in a dataset of this size. $A_1 = 90.2 \pm 3.8$, $A_2 = -0.88 \pm 0.14$, $A_3 = (1.206 \pm 0.011) \times 10^3$, $A_4 = 196.62 \pm 0.07$, $A_5 = 7.56 \pm 0.07$.

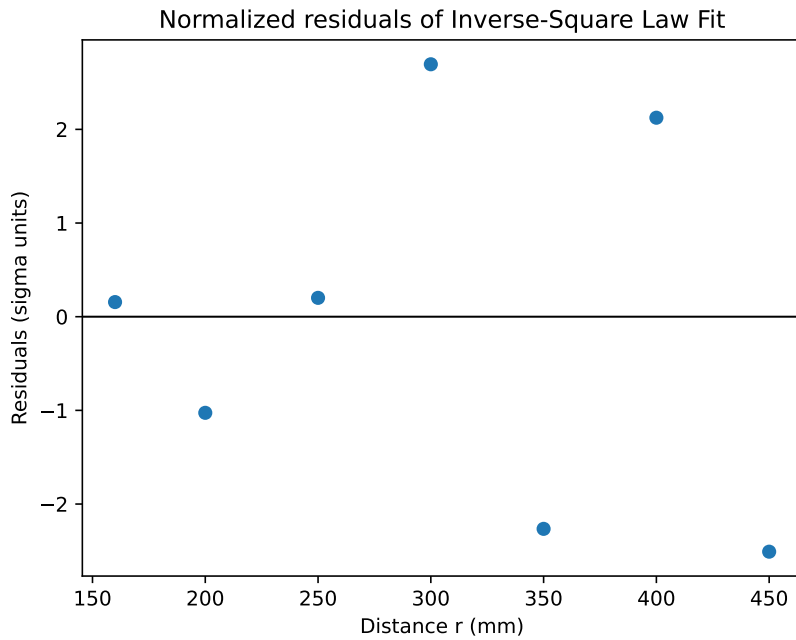


Figure 19: Normalized residuals for Inverse square fit

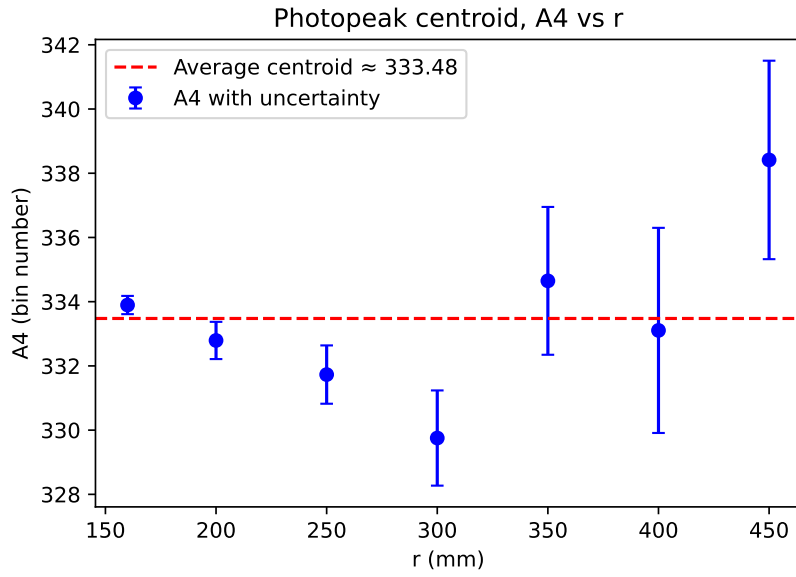


Figure 20: The values of A4 found using MLE for each distance for the second inverse square experiment. There is no systematic trend and the results are randomly scattered about the average centroid of 333.48. The gain used in this part of the experiment is different from 1st, so we can't quite say how accurate this centroid value is.

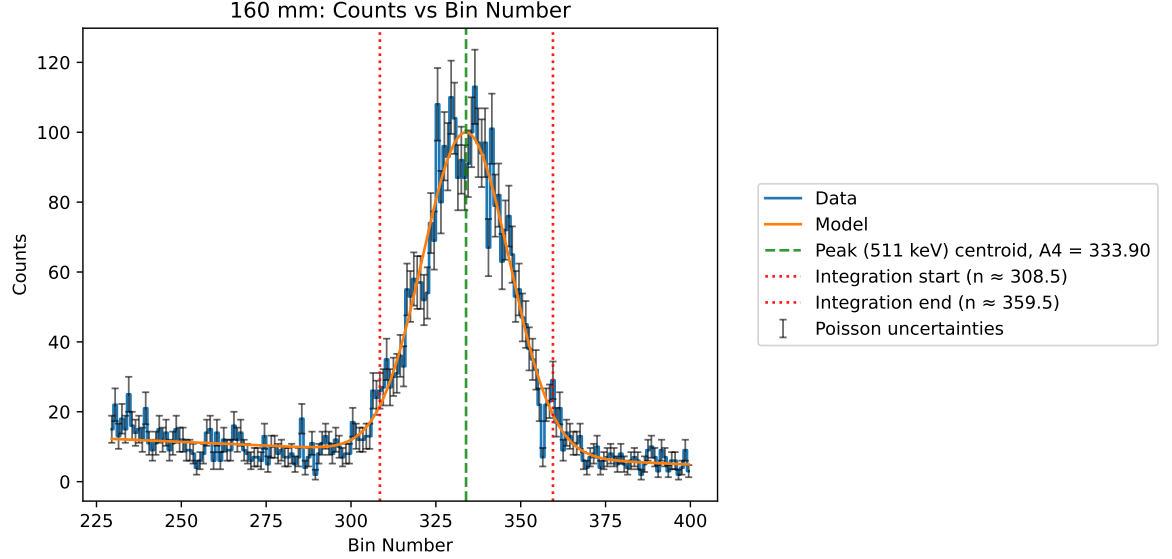
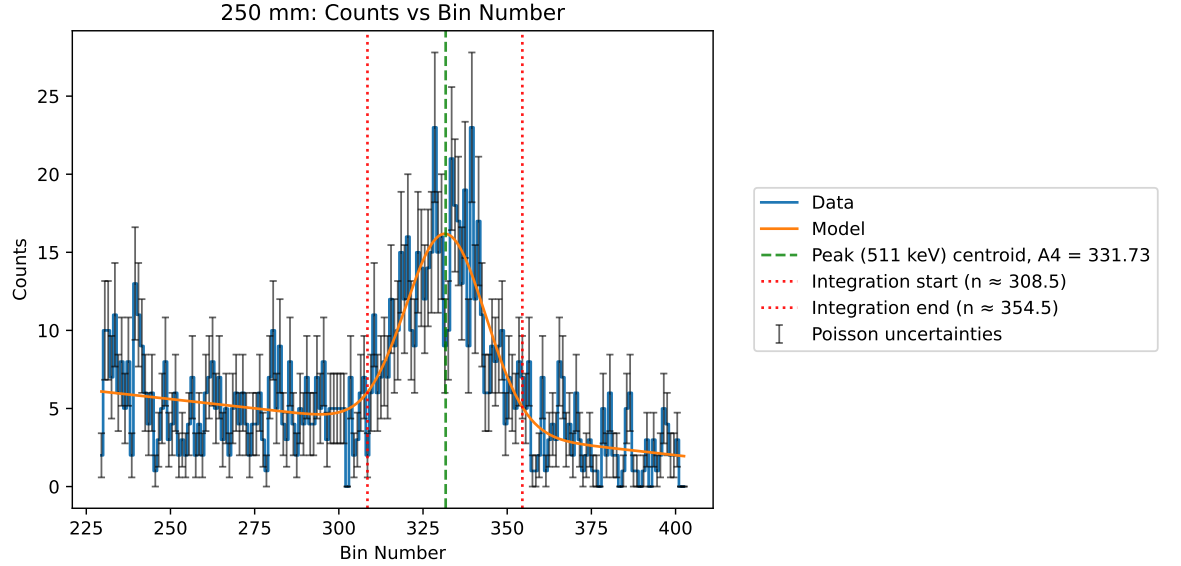
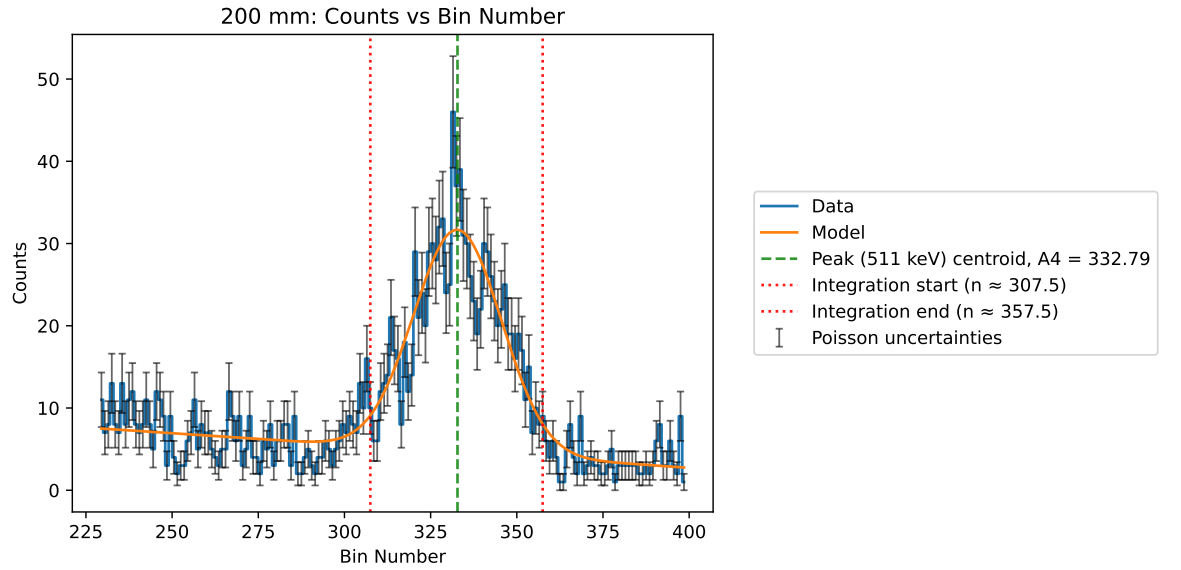


Figure 21: Counts vs Bin Number plot for detector distance $r=160\text{mm}$. Intensity (or total counts between red lines) is $I=3236 \pm 57$. Green line is the found centroid position $A4 = 333.9(3)$ using MLE. All the counts contained between the red dotted lines are added together to get intensity. The width of the integration window is set to be $\pm 2\sigma$ around peak center where σ is $A5 = 12.8(0.3)$ of the modeled gaussian. Negative log likelihood of MLE fit: 502.2192



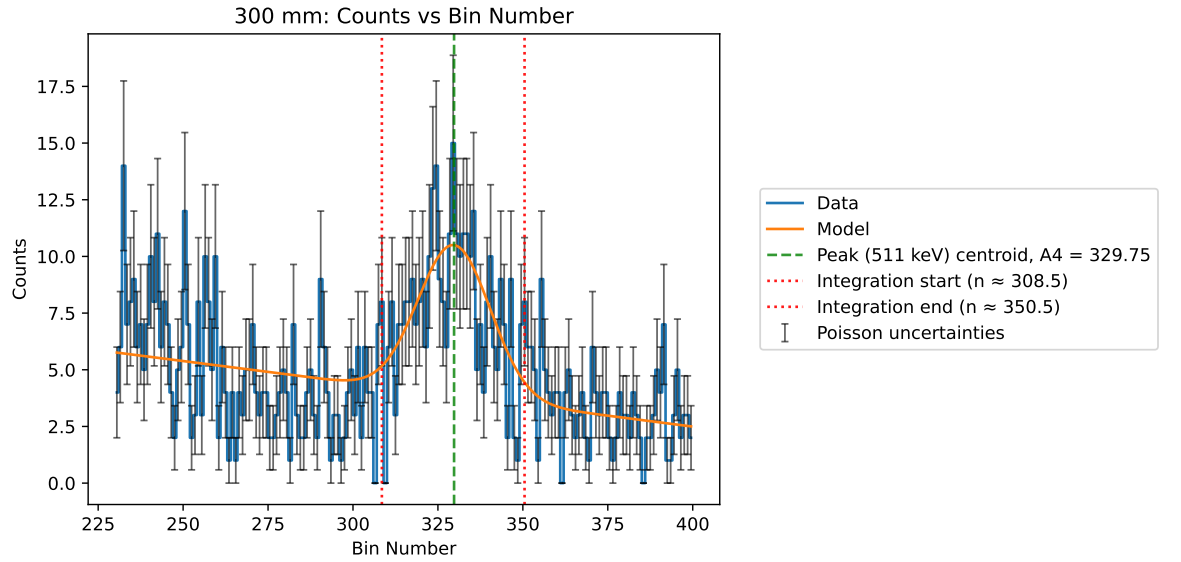


Figure 24: Counts vs Bin Number plot for detector distance $r=300\text{mm}$. Intensity (or total counts between red lines) is $I=335\pm18$. Green line is the found centroid position $A4 = 330(1)$ using MLE. All the counts contained between the red dotted lines are added together to get intensity. The width of the integration window is set to be $\pm 2\sigma$ around peak center where σ is $A5 = 11(1)$ of the modeled gaussian. Negative log likelihood of MLE fit: 381.5245

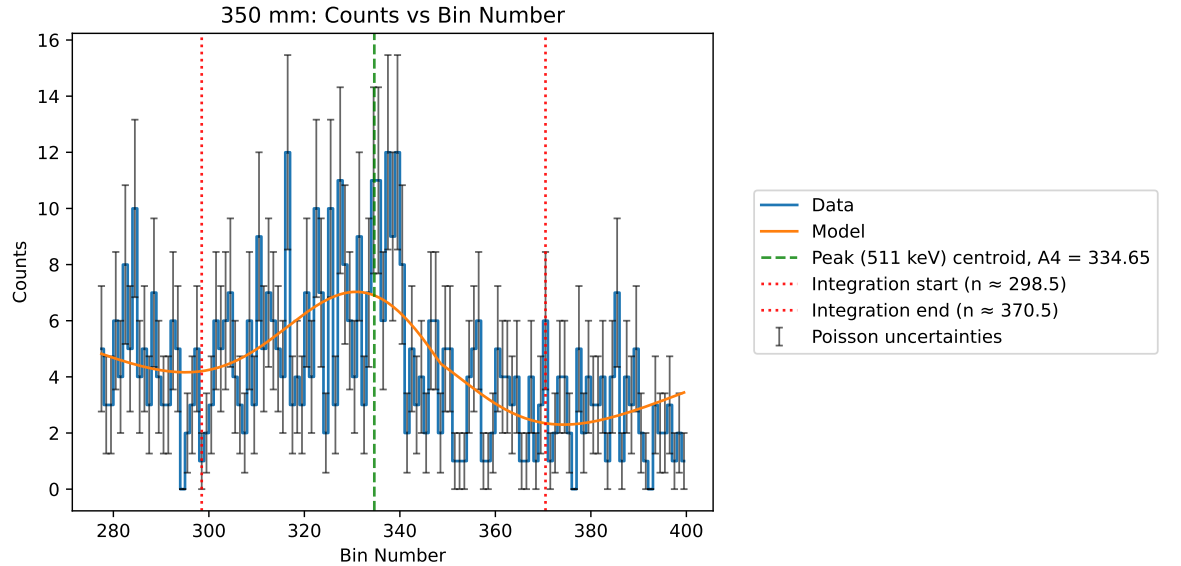


Figure 25: Counts vs Bin Number plot for detector distance $r=350\text{mm}$. Intensity (or total counts between red lines) is $I=364\pm19$. Green line is the found centroid position $A4 = 335(2)$ using MLE. All the counts contained between the red dotted lines are added together to get intensity. The width of the integration window is set to be $\pm 2\sigma$ around peak center where σ is $A5 = 18(2)$ of the modeled gaussian. Negative log likelihood of MLE fit: 268.4325

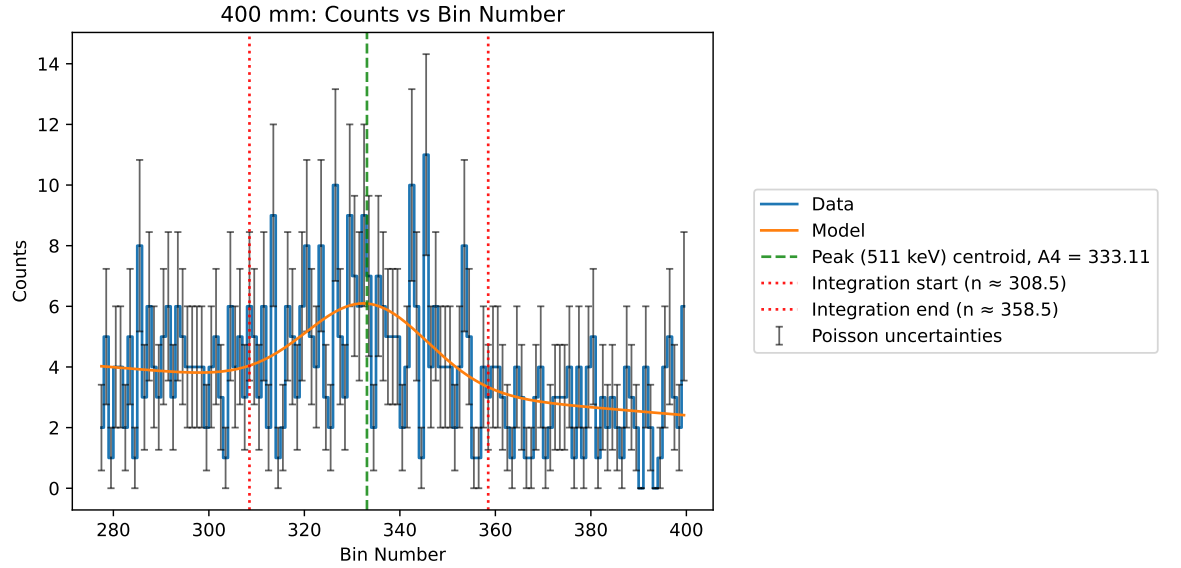


Figure 26: Counts vs Bin Number plot for detector distance $r=400\text{mm}$. Intensity (or total counts between red lines) is $I=254\pm16$. Green line is the found centroid position $A4 = 331(3)$ using MLE. All the counts contained between the red dotted lines are added together to get intensity. The width of the integration window is set to be $\pm 2\sigma$ around peak center where σ is $A5 = 13(3)$ of the modeled gaussian. Negative log likelihood of MLE fit: 249.5499

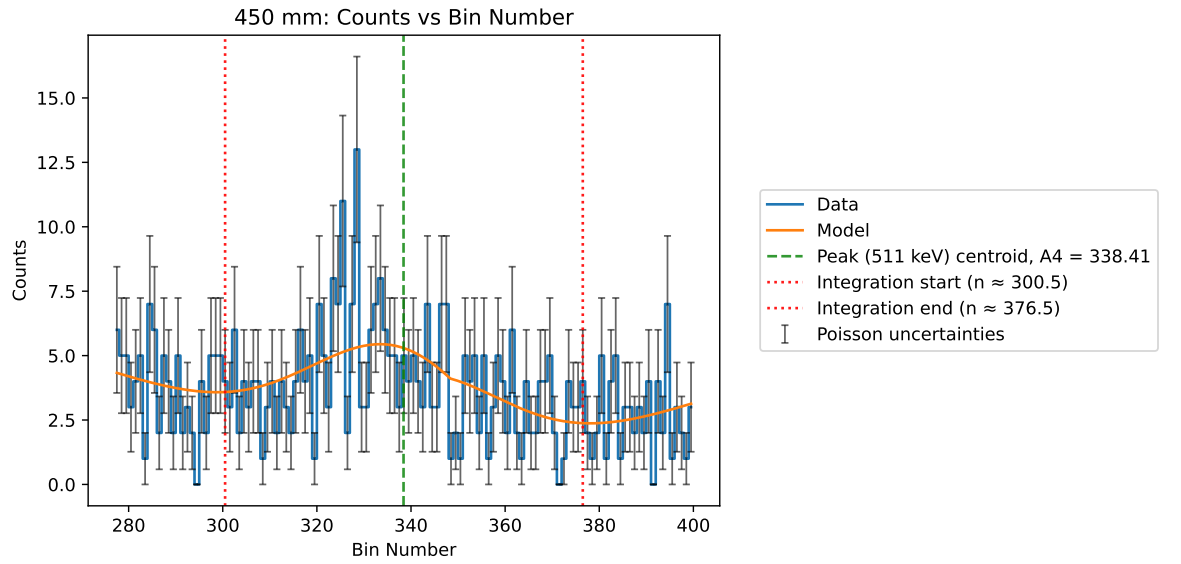


Figure 27: Counts vs Bin Number plot for detector distance $r=450\text{mm}$. Intensity (or total counts between red lines) is $I=313\pm18$. Green line is the found centroid position $A4 = 338(3)$ using MLE. All the counts contained between the red dotted lines are added together to get intensity. The width of the integration window is set to be $\pm 2\sigma$ around peak center where σ is $A5 = 19$ of the modeled gaussian. Negative log likelihood of MLE fit: 246.2170

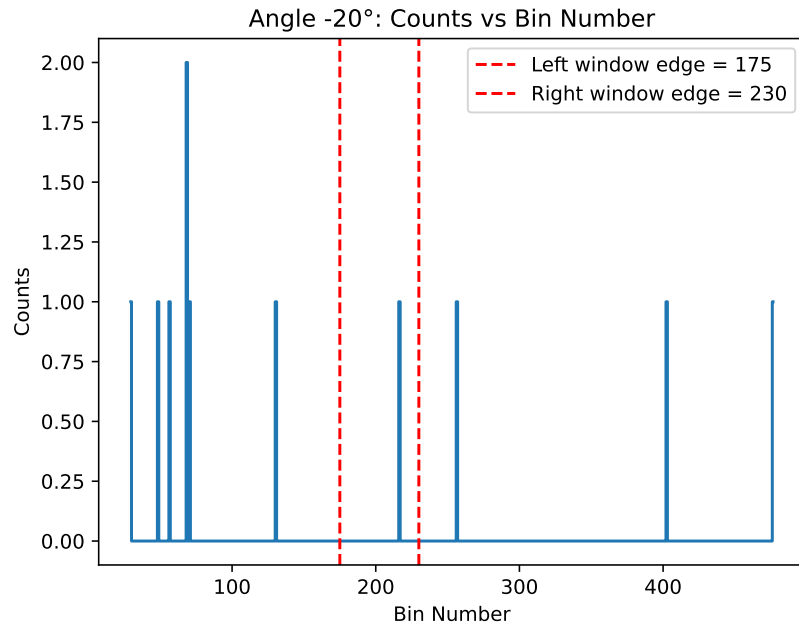


Figure 28: 511keV coincidence window for -20 degree angle of the detector. The total count of 1(1) is found by adding all the recorded counts between the red lines. Integration window is kept constant between 175 and 230 for every angle.

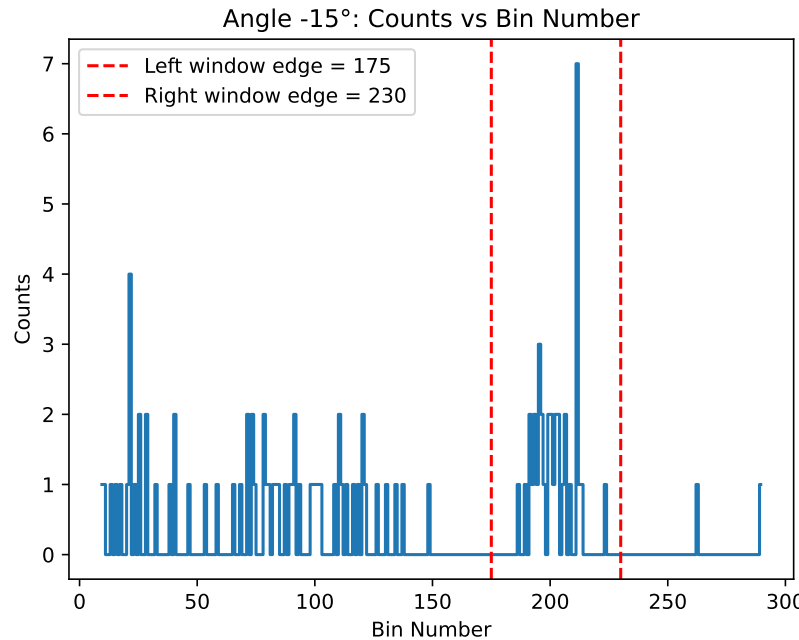


Figure 29: 511keV coincidence window for -15 degree angle of the detector. The total count of 37(6) is found by adding all the recorded counts between the red lines. Integration window is kept constant between 175 and 230 for every angle.

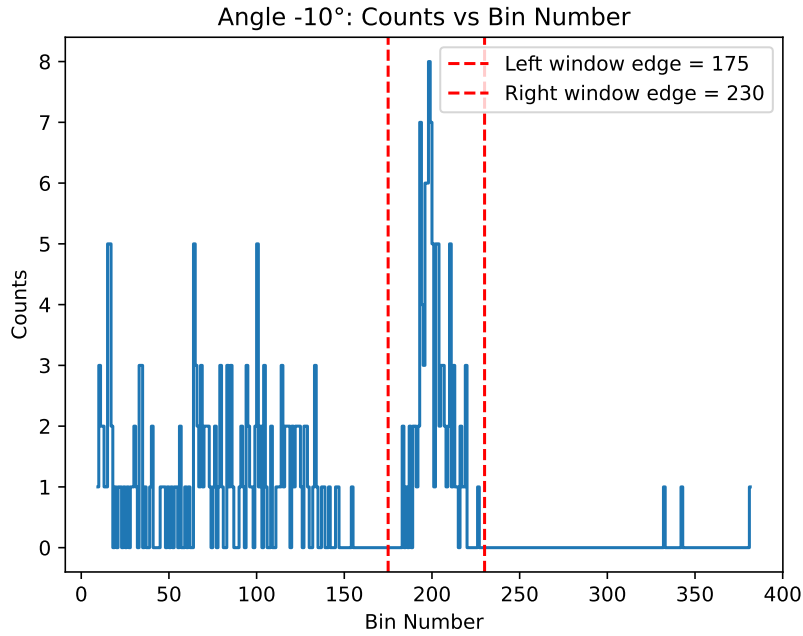


Figure 30: 511keV coincidence window for -10 degree angle of the detector. The total count of 101(10) is found by adding all the recorded counts between the red lines. Integration window is kept constant between 175 and 230 for every angle.

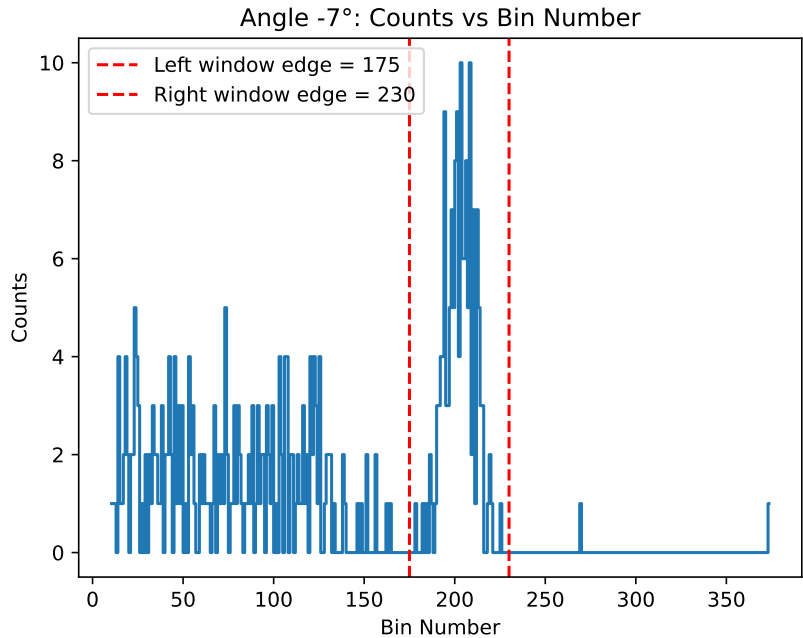


Figure 31: 511keV coincidence window for -7 degree angle of the detector. The total count of 152(12) is found by adding all the recorded counts between the red lines. Integration window is kept constant between 175 and 230 for every angle.

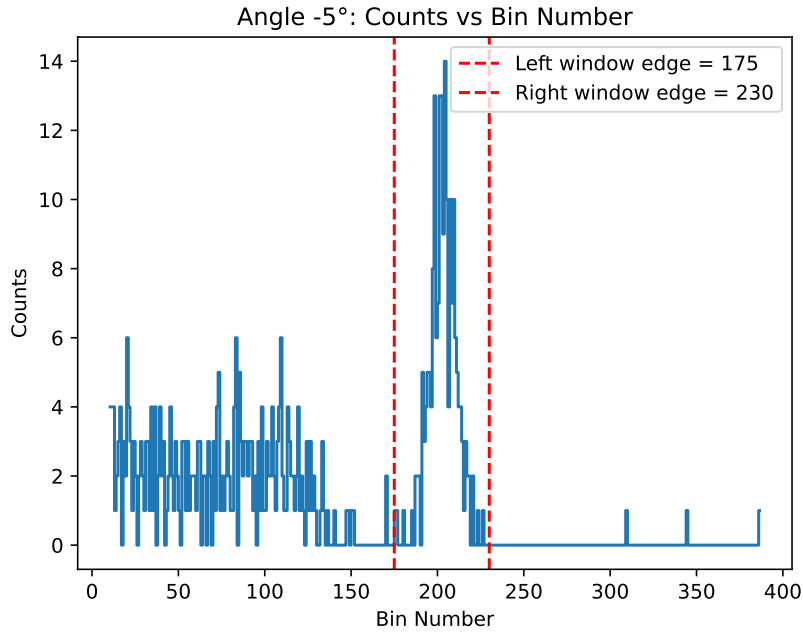


Figure 32: 511keV coincidence window for -5 degree angle of the detector. The total count of 194(14) is found by adding all the recorded counts between the red lines. Integration window is kept constant between 175 and 230 for every angle.

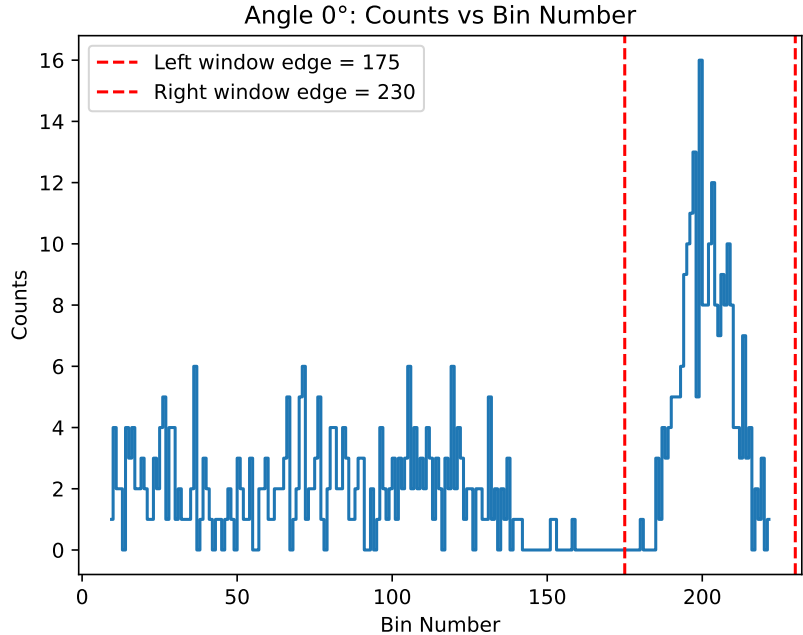


Figure 33: 511keV coincidence window for 0 degree angle of the detector. Angle 0° spectrum is also shown in the main text (Fig 13), but included here for direct comparison with the other angles. The total count of 221(15) is found by adding all the recorded counts between the red lines. Integration window is kept constant between 175 and 230 for every angle.

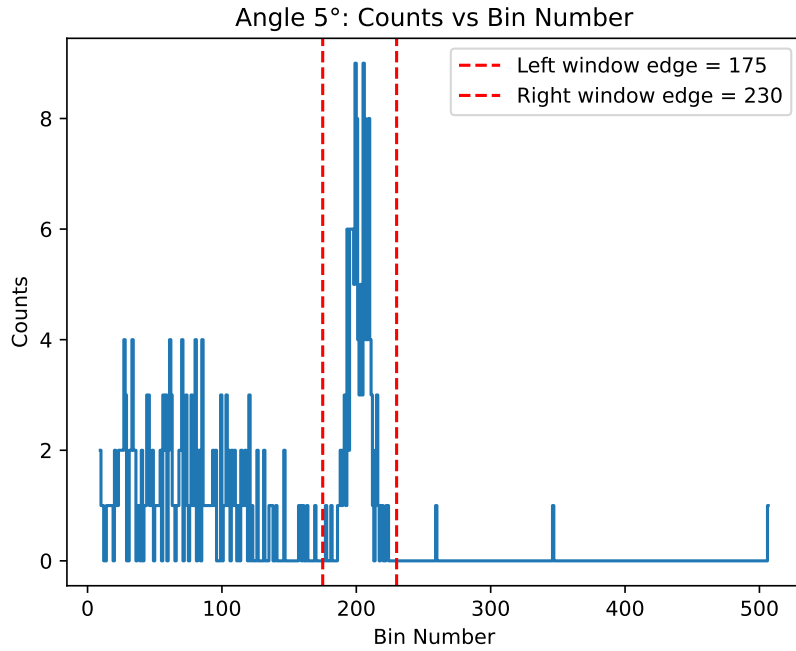


Figure 34: 511keV coincidence window for 5 degree angle of the detector. The total count of 127(11) is found by adding all the recorded counts between the red lines. Integration window is kept constant between 175 and 230 for every angle.

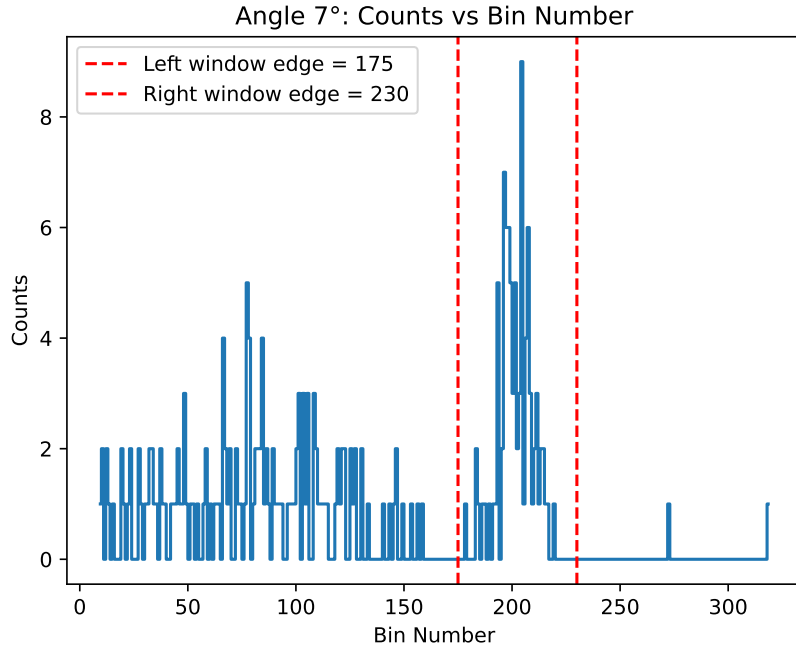


Figure 35: 511keV coincidence window for 7 degree angle of the detector. The total count of 90(9) is found by adding all the recorded counts between the red lines. Integration window is kept constant between 175 and 230 for every angle.

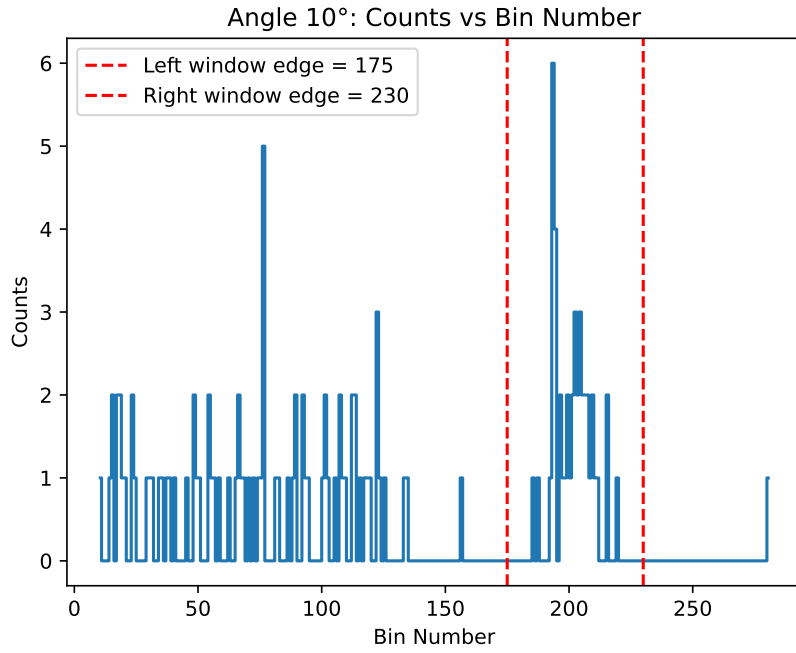


Figure 36: 511keV coincidence window for 10 degree angle of the detector. The total count of 44(7) is found by adding all the recorded counts between the red lines. Integration window is kept constant between 175 and 230 for every angle.

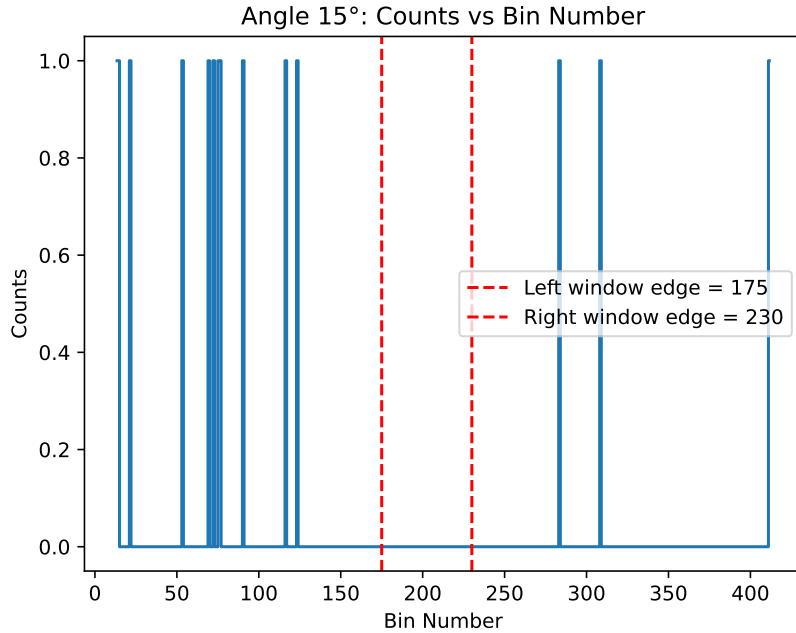


Figure 37: 511keV coincidence window for 15 degree angle of the detector. The total count of 0 is found by adding all the recorded counts between the red lines. Integration window is kept constant between 175 and 230 for every angle.

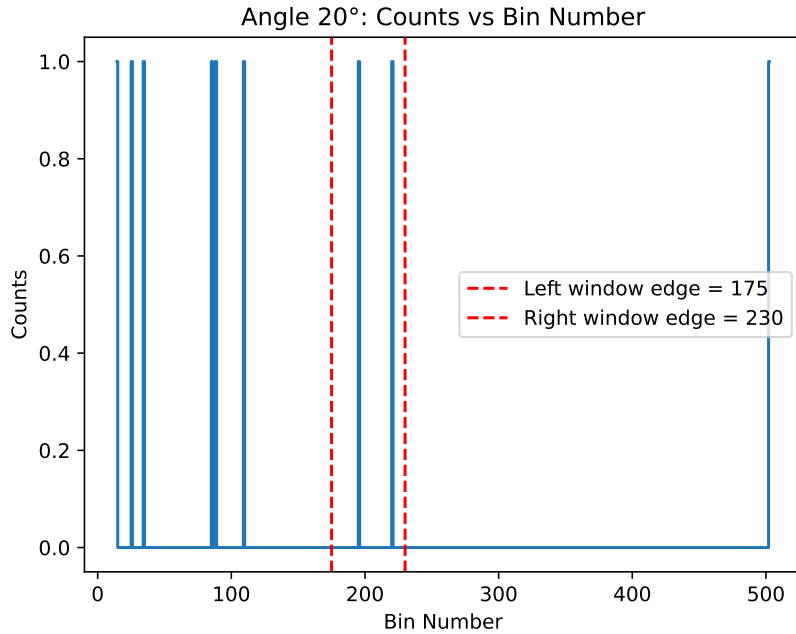


Figure 38: 511keV coincidence window for 20 degree angle of the detector. The total count of 2(1) is found by adding all the recorded counts between the red lines. Integration window is kept constant between 175 and 230 for every angle.

B Python Code Availability

All analysis scripts used in this lab report are provided in the supplementary materials. The code is written so that it can be run on any machine, as long as the folder structure and file names are preserved.

This includes the following .py files:

- `gamma_calibration.py` — MLE peak fitting and calibration, also ODR and Monte Carlo
- `inverse_square.py` — intensity vs distance plots and inverse square fitting with least squares method
- `coincidence_angles.py` — coincidence histogram generation and final gaussian fitting using MLE

The code requires:

- Python 3 (3.8+ recommended)
- The following Python packages: pip install numpy scipy matplotlib numdifftools